











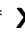















RECEIVED: March 26, 2024

REVISED: January 19, 2025

ACCEPTED: February 12, 2025

PUBLISHED: April 15, 2025

RADES axion search results with a high-temperature superconducting cavity in an 11.7 T magnet

S. Ahyoune^{},^a A. Álvarez Melcón^{},^b S. Arguedas Cuendis^{},^{a,*} S. Calatroni^{},^c
C. Cogollos^{},^d A. Díaz-Morcillo^{},^b B. Döbrich^{},^d J.D. Gallego^{},^e
J.M. García-Barceló^{},^d B. Gimeno^{},^f J. Golm^{},^{c,g,*} X. Granados^{},^h J. Gutierrez^{},^h
L. Herwig^{},^{d,i} I.G. Irastorza^{},^j N. Lamas^{},^h A. Lozano-Guerrero^{},^b
C. Malbrunot^{},^{k,l,m} W. L. Millar^{},^c J. Miralda-Escudé^{},^{a,n} P. Navarro^{},^b
J. R. Navarro-Madrid^{},^b T. Puig^{},^h M. Siodlaczek^{},^o G. T. Telles^{},^h
and W. Wuensch^{},^c

^a*Institut de Ciències del Cosmos, Universitat de Barcelona,
08028 Barcelona, Spain*

^b*Department of Information and Communications Technologies, Technical University of Cartagena,
30203 Cartagena, Spain*

^c*CERN - European Organization for Nuclear Research,
Geneva, Switzerland*

^d*Max-Planck-Institut für Physik (Werner-Heisenberg-Institut),
Boltzmannstr. 8, 85748 Garching bei München, Germany*

^e*Yebes Observatory (IGN),
19141 Guadalajara, Spain*

^f*Instituto de Física Corpuscular (IFIC), CSIC-University of Valencia,
46980 Valencia, Spain*

^g*Institute for Optics and Quantum Electronics, Friedrich Schiller University Jena,
07743 Jena, Germany*

^h*Institut de Ciència de Materials de Barcelona (ICMAB), CSIC,
08193 Bellaterra, Spain*

ⁱ*Technical University of Munich,
Arcisstraße 21, 80333 Munich, Germany*

^j*Center for Astroparticles and High Energy Physics (CAPA), Universidad de Zaragoza,
50009 Zaragoza, Spain*

^k*TRIUMF, 4004 Wesbrook Mall, Vancouver, BC V6T 2A3, Canada*

^l*Physics Department, McGill University, Montréal, Québec H3A 2T8, Canada*

^m*Department of Physics and Astronomy, University of British Columbia,
Vancouver, BC V6T 1Z1, Canada*

*Corresponding author.

ⁿ*Institució Catalana de Recerca i Estudis Avançats, 08010 Barcelona, Spain*

^o*Technical University of Darmstadt, Institute for Energy Systems and Technology, 64287 Darmstadt, Germany*

E-mail: ahyounne@fqa.ub.edu, alejandro.alvarez@upct.es,
sergio.arguedas.cuendis@cern.ch, sergio.calatroni@cern.ch,
cogollos@mpp.mpg.de, alejandro.diaz@upct.es, babette.dobrich@cern.ch,
jd.gallego@oan.es, jose.maria.garcia.barcelo@cern.ch,
benito.gimeno@uv.es, jessica.golm@cern.ch, granados@icmab.es,
jgutierrez@icmab.es, herwig@mpp.mpg.de, igor.irastorza@cern.ch,
nlamas@icmab.es, antonio.lozano@upct.es, cmalbrunot@triumf.ca,
lee.millar@cern.ch, jmiralda@fqa.ub.edu, pablonm.ct.94@gmail.com,
joser.navarro@upct.es, teresa@icmab.es,
marc.siodlaczek@est.tu-darmstadt.de, gtelles@icmab.es,
walter.wuensch@cern.ch

ABSTRACT: We describe the results of a haloscope axion search performed with an 11.7 T dipole magnet at CERN. The search used a custom-made radio-frequency cavity coated with high-temperature superconducting tape. A set of 27 h of data at a resonant frequency of around 8.84 GHz was analysed. In the range of axion mass $36.5676\,\mu\text{eV}$ to $36.5699\,\mu\text{eV}$, corresponding to a width of 554 kHz, no signal excess hinting at an axion-like particle was found. Correspondingly, in this mass range, a limit on the axion to photon coupling-strength was set in the range between $g_{a\gamma} \gtrsim 6.3 \times 10^{-13}\,\text{GeV}^{-1}$ and $g_{a\gamma} \gtrsim 1.59 \times 10^{-13}\,\text{GeV}^{-1}$ with a 95% confidence level.

KEYWORDS: Dark Matter, Dark Matter and Double Beta Decay (experiments)

ARXIV EPRINT: [2403.07790](https://arxiv.org/abs/2403.07790)

Contents

1	Introduction	1
2	RADES HTS cavity and experimental set-up	2
2.1	Cavity, HTS tapes and data acquisition	2
2.2	High field dipole magnet	4
2.3	Performance parameters	5
3	Selection and analysis of data	8
4	Results	13
5	Conclusions	15

1 Introduction

The QCD axion is a theoretically well motivated, hypothetical pseudoscalar particle beyond the Standard Model of particle physics. In addition to providing a solution to the strong CP problem [1–3], axions are an ideal candidate for dark matter [4–8]. If axions are created in a post-inflationary scenario, their present cosmic density and required mass, and their corresponding coupling to photons, can in principle be computed (see for example [9]). Numerical simulations have indicated a mass of around a few tens of μeV , with recent work pointing to higher masses [10], although with substantial uncertainties related to the production of cosmic defects and possible non-standard expansion histories of the early Universe. This motivates the search presented here and numerous other set-ups. A full list of results of haloscope searches is maintained in [11].

Various experimental techniques have been developed in the search for QCD axions as dark matter candidates. Many rely on the inverse Primakoff effect [12]. Following the original haloscope proposal by P. Sikivie [13], a radio-frequency (RF) cavity immersed in a strong external magnetic field is used to detect a resonant photon produced through the interaction of the axion and magnetic fields. Led by the ADMX collaboration [14], the parameter space around a few μeV has been probed down to the coupling values implied by the benchmark KSVZ and DFSZ models (see [15] for a recent overview).

One of the main limitations of these techniques are the noise sources determining the effective temperature at which the resonant cavity signal can be extracted. This constrains the experimental sensitivity and the limiting value of the coupling constant $g_{a\gamma}$ that can be reached by the experiment. Many ideas have been developed to reduce the noise level and to increase the signal by maximising the magnetic field, cavity quality factor and other parameters [16–22], leading to the exclusion of an impressive parameter space in the μeV region.

To search at higher axion masses, resonant cavities become smaller as the inverse proportion of the mass, reducing the sensitivity to $g_{a\gamma}$ because of the smaller volume, and also because the quality factor of the resonant cavity can be reduced with increasing frequency.

Hence, other techniques have been proposed above $\approx 50 \mu\text{eV}$, such as the MADMAX concept, a series of dielectric plates that can coherently radiate an axion field, assembled in a ‘booster’ that amplifies the signal and enables an axion scan between 50 and $100 \mu\text{eV}$ [23]. Another proposed experiment, ALPHA [24], aims to exploit plasma properties at relatively large axion masses.

The region between a couple of μeV and $50 \mu\text{eV}$ is a challenging one where cavities are reduced in size and therefore have lower quality factors due to worsened surface-to-volume ratio. In order to increase the volume at high resonant frequencies, the RADES collaboration (Relic Axion Dark matter Exploratory Set-up) has developed multi-cell cavities. A first axion search analysis was realised with a cavity array immersed in the 9 T CAST dipole magnet at CERN, and results were reported in [25].

Here we explore the prospects of increasing the quality factor of small cavities by using high-temperature superconducting (HTS) tapes, and present a search in the region centered around $36.5687 \mu\text{eV}$. The SM18 magnet at CERN, reaching a magnetic field value of 11.7 T, was used [26]. Although no frequency tuning was planned¹ in advance, a small amount of tuning occurred owing to temporal pressure variations in the helium bath inside the magnet, which led to an effective tuning of our system over a 312 kHz frequency range.

A technical article on the performance of ReBCO (Rare-earth Barium Copper Oxide) tapes that were used has been previously published [28]. We note that this is not the first report of the use of superconductors to boost quality factors of cavities: in [29] a NbTi cavity was used at 2 T, and the CAPP experiment also used YBCO tapes² [30]. The novelty of our measurement lies in the fact that the data was taken in an 11.7 T magneto static field.

In this work we also present an analysis pipeline that introduces new novelty elements like the usage of Principal Component Analysis to deal with the background noise produced by the electronics. This method showed promising results for non-standard background noise and has a lower impact on the axion line-shape compared to the standard Savitzky-Golay approach. Moreover, a modified Lorentzian analytical function was developed to better handle the power spectra produced with the new procedure.

This article is structured as follows: in section 2, we describe our measurement set-up and the concepts underlying the cavity design, and we provide the relevant cavity and environmental parameters. Section 3 details the data selection and the analysis procedure. Results of the axion search are given in section 4. The conclusions are presented in section 5.

2 RADES HTS cavity and experimental set-up

2.1 Cavity, HTS tapes and data acquisition

As reviewed in [31], previous results obtained in RADES relied on the use of cavities similar to microwave filters, i.e. with irises in between smaller sub-cavities. For this search, a quasi-cylindrical cavity shape was used. It was designed by adapting a rectangular cavity geometry

¹Such tuning is utilised at CAPP-HeT-SC, see [27].

²Although, the CAPP cavities are designed for a solenoid magnet. They, therefore, use a different mode with a different geometric factor. The resonance frequency ($\sim 6.9 \text{ GHz}$) is lower than the RADES cavity ($\sim 8.8 \text{ GHz}$).

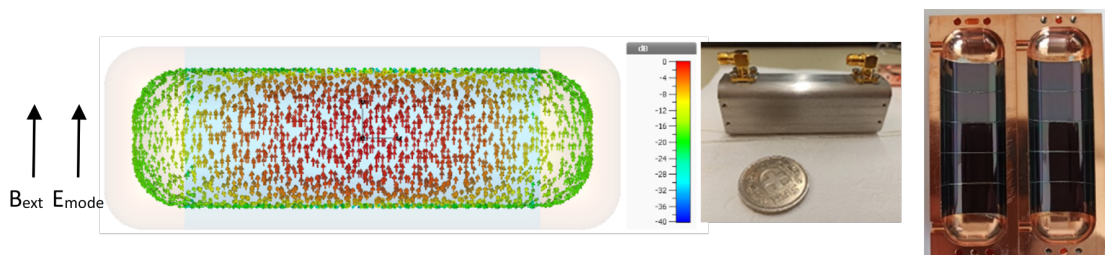


Figure 1. Left: direction of the surface currents (red showing the region of maximum surface current flow) for the TE_{111} mode (axion mode) from CST Studio Suite® simulations. Center: the cavity assembly prototype uncoated and a coin for size comparison. Right: the copper coated cavity covered with ReBCO tape. The cavity body has an inner length of 80 mm, a width of 18.8 mm, and a height of 24 mm. The corners are rounded with a radius of 9 mm.

by rounding the corners, allowing easy coating with the superconducting tapes. The left hand side (l.h.s.) of figure 1 shows a simulation of the surface currents flow in the cavity for the TE_{111} mode (axion mode) of the cavity employed in this search. The current flows are maximal along the long side of the cavity and minimal at the rounded ends of the cavity. The cavity is cut along the electrical field lines such that no currents flow across the gap of the cavity halves. The middle picture of figure 1 shows the cavity prototype assembled before coating, and the right image shows both cavity halves coated. A first layer of copper coating was applied. A high temperature superconducting tape, ReBCO provided by the company THEVA [32], with the critical magnetic field above 100 T, was taped on the inner surface omitting the rounded ends. In this region, the surface currents are shallow, and having only copper in this region affects the cavity's quality factor by less than 8 % [28].

The coating of the cavity was performed at ICMAB [33] in Barcelona where a method was developed to solder the tapes in the cavity with the substrate side facing outwards. Subsequent substrate removal exposed ReBCO to the RF field. The distribution of the superconducting ReBCO material in the cavity ensured that no RF currents were crossing the tapes. This method was previously tested on small flat samples and showed good results in performance compared to copper in magnetic fields up to 9 T, see [34, 35].

The quality factor of the cavity coated with HTS tape improved by a factor of 1.5 compared to a copper cavity and was therefore used for data taking. This value was lower than predicted. Without magnetic field, we expected an improvement of Q_0 compared to the copper reference cavity by a factor of 5-6, but we only measured an improvement by a factor of 2 without magnetic field and 1.5 with magnetic field. The reason for the lower quality factor is the bending radius of the cavity geometry as it is smaller than the critical bending radius of the tape used. As we know, coated conductors lose their superconducting properties below the critical bending radius [36, 37]. Studies to improve this value are ongoing. More details on the cavity design and coating method can be found in [28].

Here we summarise the parameters of the cavity design which are relevant to the axion search analysis, such as the volume V and the form factor C representing the overlap of the magnetic field with the resonant mode [25]. Both depend on the cavity geometry and are minimally affected by uncertainties like the thickness and quality of the soldering, fabrication

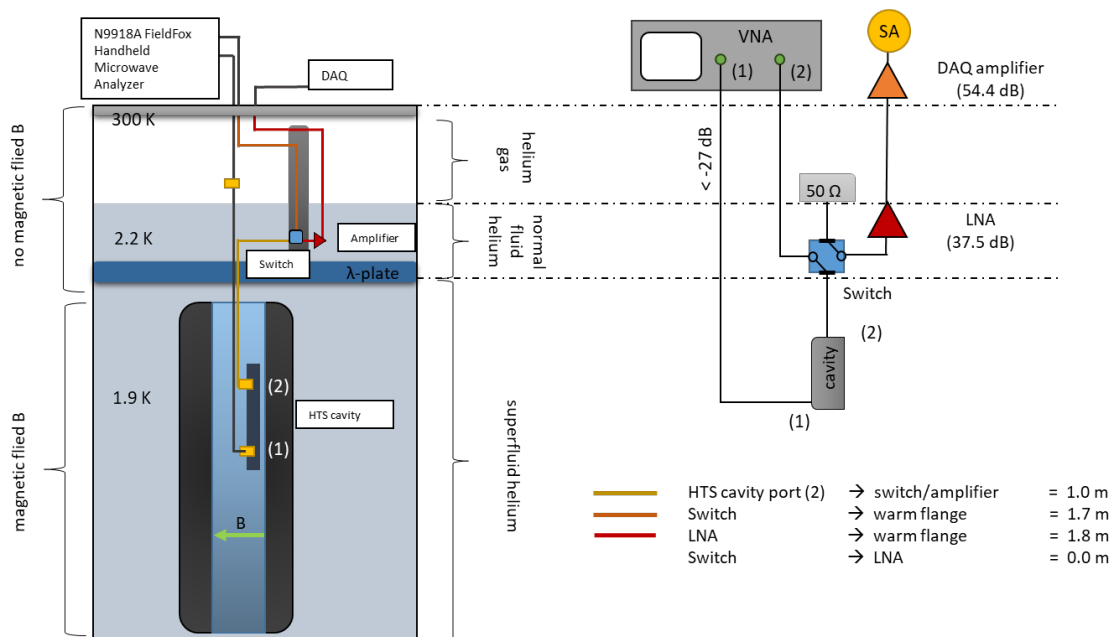


Figure 2. Left: experimental set-up for RADES axion data-taking in a 11.7 T dipole magnet at CERN’s SM18 hall in superfluid helium. Right: Wiring diagram of the set-up in the configuration for noise floor measurements to determine the noise temperature and for the quality factor measurements.

errors, and coating thickness. The cavity consists of a 316LN stainless steel main body (with fabrication uncertainties $20\ \mu\text{m}$) coated with a $30\ \mu\text{m}$ thick copper layer to which soldering tin and ReBCO tape (thickness $(40 \pm 5)\ \mu\text{m}$) were attached. Considering all these layers and the contraction of the stainless steel body by 0.3% through a temperature change from 300 K to 4 K [38], the volume was calculated to be $V = 0.0288 \pm 0.0002\ \text{L}$ and the form factor $C = 0.634 \pm 0.001$ using simulations in CST Studio Suite® [39].

For data-taking, the cavity was connected to a cryogenic low noise amplifier from Low Noise Factory of type LNF-LNC6-20C [40], which was connected to the data acquisition system (DAQ) from TTI Norte [41]. The DAQ consists of an analog and a digital stages. The analog part amplifies the input signal with a 54.4 dB LNA and then converts it to an intermediate frequency centered at 140 MHz using a Local Oscillator (LO). The digital stage has a bandwidth of 12 MHz with a bin resolution of 4577 Hz, see [25, 42].

2.2 High field dipole magnet

The HTS cavity was immersed in the bore of a 2-m long dipole magnet in a single coil configuration which can reach magnetic fields higher than 11 T; for more details see [26]. Another copper-coated cavity of the same design was concurrently installed and served as a “monitoring” cavity. A Hall sensor (Arepoc HHP- NPs) attached to the cavities assembly allowed the alignment of the cavities in the magnetic field before the cool-down of the magnet and measurements of the field during operation. One copper cavity surface was aligned with the Hall probe, and the HTS cavity was lined up with the copper cavity. At ambient conditions, the static magnetic field at a very low current was surveyed with the Hall probe to find the axis of the magnetic field. We expect less than 5 % deviation of the field compared to

the maximum B-field. This deviation is taken into account in the errors. During data taking, the magnet was kept at a current of $I = 11\,850\text{ A}$, corresponding to a magnetic field $B = 11.7 \pm 0.1\text{ T}$ which is constant along the cavity. The magnet and the cavity assembly were inserted in a cryostat filled with liquid helium. The l.h.s. of figure 2 shows the experimental set-up. The helium in the magnet bore was superfluid and the cavities were kept at a temperature of $T = 1.897 \pm 0.008\text{ K}$ during data-taking. A Cernox resistance sensor was attached to each cavity for temperature measurement. The fluid around the cavity ensured the temperature was constant over the cavity length.

During the data-taking period the pressure of the system fluctuated over a range of $p = 1.27$ to 1.36 bar , causing a slight variation of the helium relative dielectric constant, $\varepsilon_r(1.9\text{ K}, 1.36\text{ bar}) = 1.058$ (calculated from HEPAKTM [43]) of less than 0.01 %. This resulted in a tuning of the resonant frequency over a range of 312 kHz. The pressure during the data taking depended on installations in the SM18 hall at CERN and the resulting environmental noise conditions, and was most stable during the weekend and at night, when most of the data were acquired.

2.3 Performance parameters

Besides volume and form factor, essential performance parameters for the axion search are the quality factor, coupling, amplification, and noise temperature. To enable a direct measurement of these parameters, a microwave switch was installed in the set-up.

The cavity has two ports, while one port is weakly coupled (terminated for the axion search - port (1)), we aim for critical coupling at the second port (strongly coupled - port(2)), i.e., a coupling between the cavity and the receiver chain of $\beta = 1.0$. To minimise the attenuation of the signal coming from the cavity, the strongly coupled port was chosen to be as close as possible to the amplifier. For this reason, the top port in figure 2 is the strongly coupled port. This port was connected to a switch by a copper RF cable of $l = 1.0 \pm 0.1\text{ m}$ length. A cryogenic low-noise amplifier was connected directly to the switch allowing to bypass the amplifier to perform resonant frequency and quality factor measurements and obtain Q_L and β . The quality factor and coupling were monitored on two subsequent days before the data-taking using a vector network analyser (VNA), this will be labelled as calibration data. By measuring the transmission coefficient S_{21} a loaded quality factor of $Q_L = 36\,656 \pm 1832$ was obtained³ and a coupling of $\beta = 0.81 \pm 0.04$ at 11.7 T by measuring the reflection coefficient S_{11} [44]. Both values remained constant within their error bars for a frequency range of 295 kHz during the period we monitored the Q-value.

Figure 3 l.h.s. shows one set of S-parameter of the calibration measurements that were performed in the experimental set-up in comparison to simulations. They are in good agreement, which was necessary since the form factor was calculated using simulations. Moreover, the neighbouring resonances are at 7.97 GHz and 9.05 GHz. Any type of mode mixing can be excluded. Figure 3 r.h.s. shows the unloaded quality factor versus magnetic field, which displays no hysteresis during ramp-up and ramp-down, demonstrating the robustness of the magnetic flux configuration at these high magnetic fields where the HTS is fully saturated.

³A 5% uncertainty was taken for Q_L and β to account for the systematic uncertainties of the system.

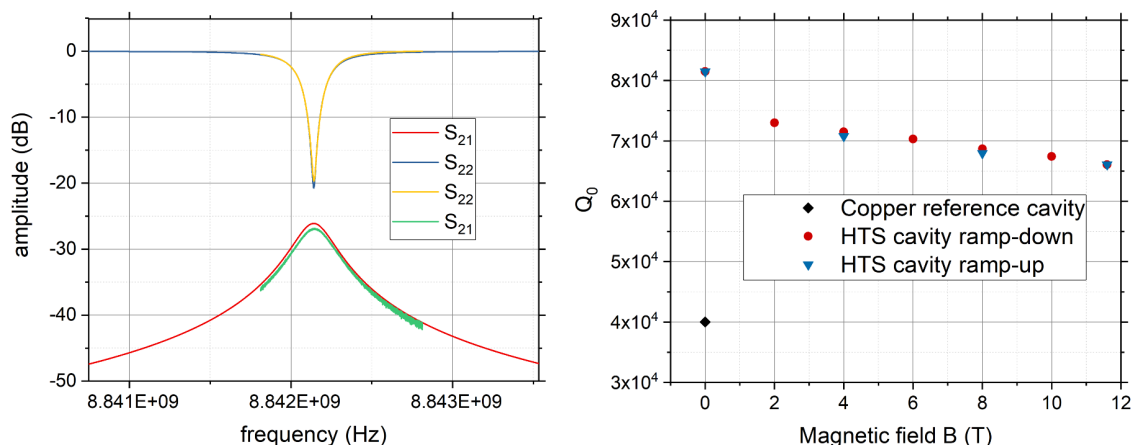


Figure 3. Left: comparison of the measured S-parameters (transmission S_{21} - green, reflection S_{22} - yellow) and the simulated S-parameters (transmission S_{21} - red, reflection S_{22} - blue) of the HTS tape cavity. The measured S-parameters were used for quality factor and coupling calculation of the HTS cavity during the calibration measurements at 1.9 K and 11.7 T. For the plot, cable losses were calibrated after the measurement. Right: unloaded quality factor versus magnetic field for the HTS tape cavity at 1.9 K for ramp-down and subsequent ramp-up in comparison to a copper coated reference cavity of the same shape at zero magnetic fields.

To determine the noise temperature of the system a direct power method was chosen. Therefore, it was important to know the gain of the low noise amplifier (LNA). Thanks to the switch, it was possible to inject an RF signal in the cavity and measure the outgoing power at the other port. This could be done by going through the amplifier once and by-passing it for a second measurement. Since the cables in both lines are almost of the same length (1.70 m for the bypassing line versus 1.80 m for the amplifier line) it allowed good measurements of the gain, which was measured to be 37.4 ± 0.9 dB.

To measure the noise floor of the cryogenic low noise amplifier (LNA), the LNA was terminated with a 50Ω cold load that was connected to the RF switch as shown in the wiring diagram in the right hand side (r.h.s.) of figure 2. For this measurement, another room temperature amplifier (54.4 dB) connected between the LNA and spectrum analyser (SA) had to be added to amplify the RF signal above the noise floor of the spectrum analyser. A wiring diagram for the noise floor measurement of the LNA, by-passing the cavity, is shown in the right hand side (r.h.s.) of figure 2. The noise floor was measured to be -71.1 ± 0.2 dBm. With this value the noise power P_{amp} of the LNA taking into account the attenuation from the cables and the gain provided by the amplifiers was calculated using equation (2.1) to $P_{\text{amp}} = 157.8 \pm 1.9$ dBm which corresponds to a noise power density of $P_d = 0.05$ dBm Hz $^{-1}$.

$$P_{\text{amp}}[\text{dBm}] = \text{NF} - \text{Gain}_{\text{LNA}} - \text{Gain}_{\text{DAQ}} + \text{Cables}_{\text{cryo}} + \text{Cables}_{\text{warm}} \quad (2.1)$$

A list of the contributions for this calculation can be found in table 1.

The cable attenuation at 300 K and 10 GHz is quantified by the vendor as 1.45 dB m $^{-1}$ [45]. In this set-up, the cables have a temperature gradient from 1.9 K to 300 K and the measurement was performed at frequencies below 9 GHz. Therefore the cable attenuation is expected to

Parameter	Value	Unit
Noise floor	-71.1 ± 0.2	dBm
Gain LNA	37.4 ± 0.9	dB
Gain DAQ amplifier	54.4 ± 0.3	dB
Cryogenic cables	-3.1 ± 0.4	dB
Warm cables	-2.0 ± 0.1	dB
Noise power P_{amp}	-157.8 ± 1.9	dBm

Table 1. List of contributions used for noise power P_{amp} calculation with direct noise measurement method.

be smaller than given in the datasheet, especially in the 1.9 K region. During operation, the cable attenuation for the amplifier line could not be measured, but the S-parameters from the line cavity port (2) - switch - VNA gave an estimate of the attenuation. An attenuation of 3.1 ± 0.4 dB for the 3.7 m long cable chain was measured. The attenuation of the cable chain including the amplifier was estimated to have the same attenuation, which is a very conservative approach. Finally, the amplifier noise temperature was calculated using equations (2.2) and (2.3).

$$P_{\text{amp}}[\text{W}] = 1/1000 \cdot 10^{\frac{P_{\text{amp}}[\text{dBm}]}{10}} \quad (2.2)$$

$$T_{\text{amp}} = \frac{P_{\text{amp}}}{k_b \cdot \Delta\nu} \quad (2.3)$$

Where k_b is the Boltzmann constant and $\Delta\nu$ the bandwidth corresponding to 3 kHz for our measurement. The noise temperature of the LNA was calculated to be $T_{\text{amp}} = 4.1 \pm 0.8$ K. This value is in good agreement with the noise temperature given in the datasheet of the amplifier (3.5 K at 9 GHz) [40].

To take into account the contribution of the cable from the cold attenuator to the amplifier (90 mm length, losses of 0.2 dB), the formula for the noise temperature of the amplifier is given by:

$$T_{\text{amp-new}} = (L - 1)T_{\text{amb}} + T_{\text{amp}}, \quad (2.4)$$

where T_{amb} is the physical temperature of the cable (2.1 K), and L is its linear loss factor (1.05). The new noise temperature of the amplifier would be 4.2 K.

To obtain the system noise temperature the contributions of the physical temperature of the cavity ($T_{\text{cav}} = 1.9$ K) and the thermal noise attenuated by 27 dB injected through the weakly coupled port ($T_{\text{coupling}} = 300 \text{ K}/500 = 0.6$ K), need to be added to the amplifier noise temperature [46].

$$T_{\text{sys}} = T_{\text{amp-new}} + T_{\text{cav}} + T_{\text{coupling}} \quad (2.5)$$

This results in a system noise temperature of $T_{\text{sys}} = 6.7 \pm 0.8$ K. The total noise temperature is primarily determined by the noise temperature of the cryogenic amplifier, as its high gain minimizes the contribution of subsequent stages.

Due to the fact that access to the experimental facility was restricted in certain measurement intervals, it was necessary to measure the described performance parameters outside the data-taking interval.

3 Selection and analysis of data

The data used for this analysis were collected between the 13th and 15th of November 2021. A power spectrum was taken every $t = 5.36868\text{ s}$ and consists of 2622 frequency bins in a 12 MHz span centred at the intermediate frequency (IF) of 140 MHz. The LO frequency can be set using the following equation:

$$\text{IF} = x_0 - \text{LO}, \quad (3.1)$$

where $x_0 \approx 8.842\text{ GHz}$ is the centre frequency of the cavity. The LO frequency was switched once per hour between two different LO frequencies ($l_1 = 8.700481644\text{ GHz}$ and $l_2 = 8.704143756\text{ GHz}$). This was done in order to sample amplifier noise that was later used to remove part of the electronic background as described below. With these two LO values we made sure there was enough separation between the position of the cavity peak at the IF range as shown in the l.h.s. of figure 5. For this analysis we used approximately 27 h at l_1 and 22 h at l_2 .

The analysis in this paper was designed following a special procedure with the goal of removing the electronic systematic of the read-out system. The analysis steps are outlined as follows:

1. Division of the power spectra of l_1 by the average spectrum of l_2 .
2. With a DAQ calibration sample, characterise the cavity spectral profile, the electronic background (EB) and its time variability using Principal Component Analysis (PCA).
3. Remove the EB of the data-taking power spectra using a fit function based on a modified analytical Lorentzian function and the PCA.
4. Combine the individual spectra using a weighted sum to construct the Grand Unified Spectrum.
5. Remove the remaining systematic structure using a Savitzky-Golay (SG) fit.
6. Search for an axion by fitting its lineshape to the spectrum.
7. If no signal is observed, a 95% confidence level exclusion plot is created using Bayesian statistics.

Detailed description of steps 1, 5 and 6 can be found in [25]. In this work we will focus on the improvements made over previous analysis to remove the EB and the systematic residual.

In the off-the-shelf DAQs known to us, there is always a limit to the amount of hours that can be combined before a systematic residual becomes larger than the statistical noise fluctuations. Having a good control and understanding of this systematic residual is

fundamental for the axion signal sensitivity to be limited by the statistical noise fluctuations rather than the EB.

Our 12 MHz span for a single power spectrum is larger than the average span of other axion experiments which is between 1 and 5 MHz. This allowed for the cavity response at the two different IF to be completely covered within these 12 MHz, as shown in the l.h.s. of figure 5. This let us do the first step of the analysis pipeline. Moreover, l_1 and l_2 did not need to be tuned during the data-taking period because the tuning range of the cavity centre frequency was completely covered by the frequency span of the DAQ.

However, it turned out that the custom-made electronics of our DAQ imprinted a characteristic wave-like EB (see the l.h.s. of figure 5) to the signal. The standard axion search analysis steps described in [47] could not account for that EB and the associated systematic residuals produced by the DAQ, in particular its time variations which prevent a simple calibration and removal. We therefore investigated other ways of handling the correction of these structures, and we opted for using PCA.

To characterise this EB of the DAQ, we took calibrating data using a noise source as an input signal. The gain curve was computed using the following equation:

$$G = \frac{P_h - P_c}{T_h - T_c}, \quad (3.2)$$

where P_h and P_c are the powers measured by the DAQ when the noise source was on and off, respectively, and T_h and T_c are the noise equivalent temperatures for the noise source on and off, respectively.

A set of 13 gain curves was produced to perform the PCA, a statistical technique that performs a linear transformation of the original data into a new coordinate system where the variation of the data is described by its Principal Components [48]. The gain curve measurements were done outside the SM18 environment after the data-taking period was finished. Figure 4 shows the PC of the EB. Time variations of the EB during the data-taking period can then be modelled as a linear combination of the PC. A SG filter [49] (with $W = 141$ points and a polynomial degree $N = 3$) was applied to the PC to smooth out the noise fluctuations in the measurements to produce the gain curves. The optimum SG fit parameters (W , N) were identified by scanning the parameters and comparing the residuals distribution for each combination of parameters with an expected Gaussian distribution.

Note that the spectra used to create the PC and characterise the EB were produced using independent sets of data taken when the DAQ was isolated from the rest of the experimental set-up. This is an advantage compared to the previous axion search in RADES, where the EB is removed only with a SG fit applied directly on the data: the PCA helps remove systematics without causing any attenuation of any possible axion signal.

In ideal conditions, the resonance peak of a haloscope can be described using a Lorentzian function. However, our data could not be fitted in this way. Instead, we noticed the data could be fitted by a Lorentzian function multiplied by a linear term (see equation (3.3)). We attribute this modified cavity resonance profile to the presence of reflecting waves between the cavity and the low noise amplifier (LNA) due to the lack of a RF isolator between the two of them, although we were unable to positively identify the source of this modification. A linear term multiplying the Lorentzian function is used, which is found to fit the measured

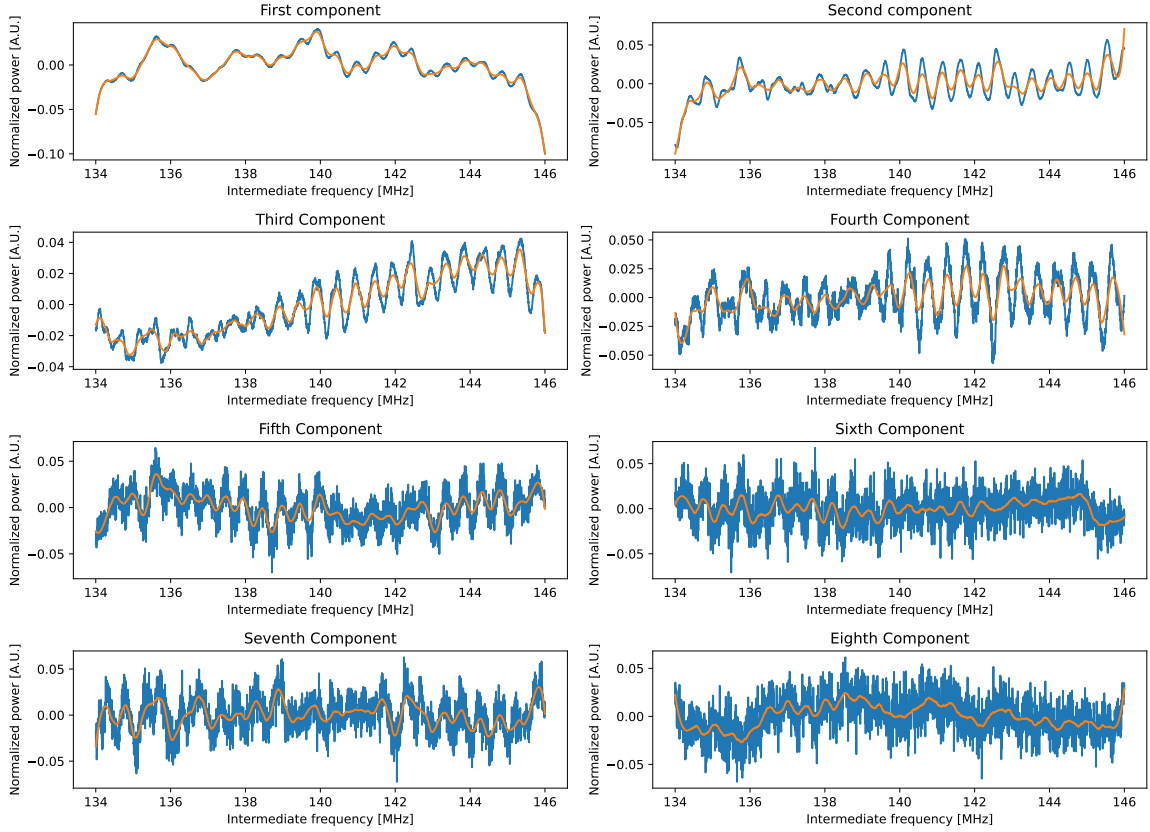


Figure 4. In blue the first eight principal components of the DAQ gain curve. In orange the SG fit applied to them to smooth out the noise fluctuation.

profile perfectly as far as the measurement noise allows us to tell. Following this approach, each spectrum obtained after performing step 1 of the analysis, denoted as δ_{ik}^d , where i represents the i -th spectrum and k the physical frequency ($\text{PH} = \text{IF} + l_1$), was fitted with the following function:

$$f(x) = \left(\left(1 + \frac{A_0(1 - (\frac{x-x_0}{D_1}))}{1 + (\frac{x-x_0}{D_1})^2} \right) / \left(1 + \frac{A_1(1 - (\frac{x-x_1}{D_2}))}{1 + (\frac{x-x_1}{D_2})^2} \right) \right) \times (a_0 + a_1 \cdot x + p_1 \cdot g_1^{\text{PC}}(x) + p_2 \cdot g_2^{\text{PC}}(x) + \dots + p_7 \cdot g_7^{\text{PC}}(x)), \quad (3.3)$$

where the first two terms describe the modified Lorentzian functions measured at the two LO frequencies. The amplitudes are given by A_0 and A_1 , x_0 and x_1 are the centre frequencies for the two LOs, and D_1 and D_2 are their full widths at half maximum. The $g_s^{\text{PC}}(x)$ ($s = 1, \dots, 7$) are the SG fits of the PC (see orange line of figure 4). The p_s represent the weights given to each PC.

To make sure that the fit gave meaningful values for x_0 and Q-loaded, the calibration measurements (see figure 3) were used to compare the values measured by the VNA (which are described by a standard Lorentzian function with a well known physical model) with the ones given by the fit function. The centre frequency x_0 was similar for both Lorentzian models, while the Q-value of the modified Lorentzian was higher by an offset of around 9500.

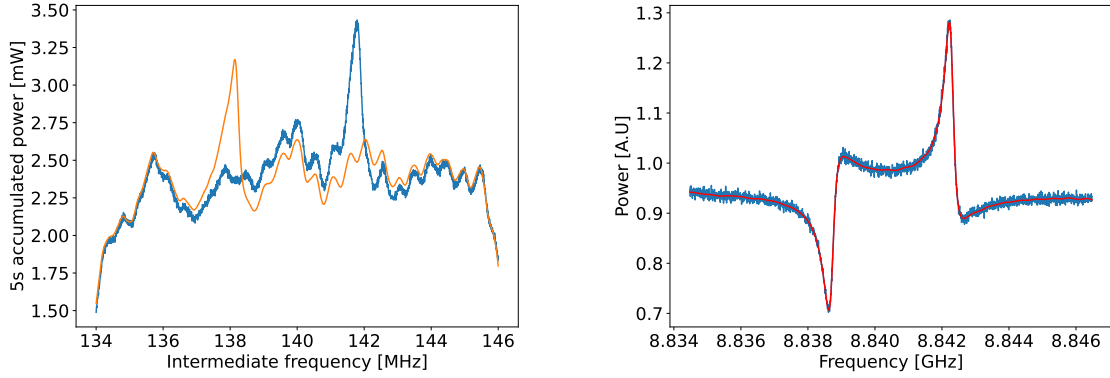


Figure 5. Left: typical spectra for two different LO frequencies ($l_1 = 8.700\,481\,644$ GHz in blue and $l_2 = 8.704\,143\,756$ GHz in orange). Upon changing the LO frequency, the cavity resonance peak changes position in the IF frequency. Right: in blue an example of a δ_{ik}^d spectrum obtained by the division of two spectra taken at two different LO frequencies. In red the fit function produced by equation (3.3).

The Q-values given by the fit during the calibration were similar within uncertainties to the ones measured during the data-taking period. Since the offset is known, the real physical Q-loaded during data-taking corresponds to the value measured with the VNA during the calibration and this value was the one used for the exclusion limit described below.

The r.h.s. of figure 5 shows a fit function on top of one δ_{ik}^d spectrum. The δ_{ik}^d spectra are then divided by their corresponding fit function and centred at zero:

$$\delta_{ik}^n = \frac{\delta_{ik}^d}{f_{ik}} - 1. \quad (3.4)$$

If the fit is able to remove the EB, the δ_{ik}^n spectra should be samples of a Gaussian distribution centred at $\mu = 0$ and standard deviation $\sigma^t = 1/\sqrt{\Delta\nu \cdot t}$, where $\Delta\nu = 4578$ Hz is the resolution bandwidth of a single bin and $t = 5.36868$ s is the integration time of each spectrum. The l.h.s. of figure 7 shows the histogram of all δ_{ik}^n/σ^t .

As described in section 2, pressure changes inside the cryostat resulted in a tuning range of 312 kHz.⁴ To obtain an adequately weighted spectrum accounting for this tuning, the spectra were re-scaled by Lorentzian functions denoted L_{ik} ⁵

$$L_{ik}(x) = \frac{1}{1 + 4Q_L^2(x/x_0 - 1)^2}, \quad (3.5)$$

where the centre frequency used is the x_0 value given by the fit to each individual spectrum (see equation (3.3)), and Q_L is the loaded quality factor, with the value of $Q_L = 36656$ measured with the VNA during the calibration measurements done before the data-taking

⁴Almost 85 % of the time was taken within a narrower effective tuning range of 55 kHz.

⁵Note that the Lorentzian L_{ik} is normalised to 1 at $x = x_0$, to match the axion power P_a given in equation (4.5) at the resonance frequency.

period as detailed in section 2. The re-scaled δ_{ik}^s and standard deviation σ_{ik}^s were computed as:

$$\delta_{ik}^s = \frac{\delta_{ik}^n}{L_{ik}}, \quad (3.6)$$

$$\sigma_{ik}^s = \frac{\sigma_i^n}{L_{ik}}. \quad (3.7)$$

Here, the noise of each spectrum i , σ_i^n , is not the theoretical value σ^t , but is instead computed directly from the dispersion of the frequency bins in each spectrum; in practice there are small jumps in this dispersion at the level of $\sim 2\%$ caused by small systematics, but in any case changing this noise does not change our results significantly.

The weighted Grand Unified Spectrum (GUS), shown in the l.h.s. of figure 6 can be computed using the weighted sum of the power spectra [47]:

$$\delta_k^g = \sum_i \delta_{ik}^s \cdot w_{ik}, \quad (3.8)$$

where the weights w_{ik} are given by

$$w_{ik} = \frac{(\sigma_{ik}^s)^{-2}}{\sum_{i'} (\sigma_{i'k}^s)^{-2}}. \quad (3.9)$$

The standard deviation of the weighted GUS spectrum is similarly computed as

$$\sigma_k^g = \sqrt{\sum_i (\sigma_{ik}^s)^2 \cdot w_{ik}^2}. \quad (3.10)$$

However, σ_k^g needs to be corrected due to the fact that on the first analysis step the spectra are divided by the average spectrum of l_2 , which has its own noise fluctuation $\sigma^{l_2} = 1/\sqrt{\Delta\nu \cdot t^{l_2}}$, where $t^{l_2} = 22$ h is the total time taken for the spectra with local oscillator l_2 . The corrected standard deviation is given by:

$$\sigma_k^{g*} = \sqrt{(\sigma_k^g)^2 + (\sigma^{l_2})^2}. \quad (3.11)$$

For the frequency range of interest (see section 4), we find that the GUS that is obtained with this procedure still contains a systematic which dominates over the statistical fluctuations, originating from residual EB (see l.h.s. of figure 6). A SG fit (labelled δ_k^{SG}) with $W = 27$ and $N = 3$ was done to characterise this residual. The residual was removed to create the final weighted GUS ($\delta_k^f = \delta_k^g - \delta_k^{\text{SG}}$). The r.h.s. of figure 6 shows the result after the systematic residual was removed. The histogram of the normalised spectrum (δ_k^f/σ_k^{g*}) exhibits the expected Gaussian distribution (see r.h.s. of figure 7).

This procedure induces an attenuation and distortion of the axion signal (see section 4), but the effect is smaller than the one evaluated in our previous analysis [25], where the SG fit was done with $W = 15$ and $N = 3$. A larger window moves the cut off frequency of the SG filter to lower frequencies reducing the attenuation of the axion signal [42], an improvement that is obtained thanks to the PCA that we have applied. Moreover, with this new analysis approach the EB and systematic residual removal was achieved for the whole frequency span of our DAQ. This allows the analysis procedure to work on a broader frequency range.

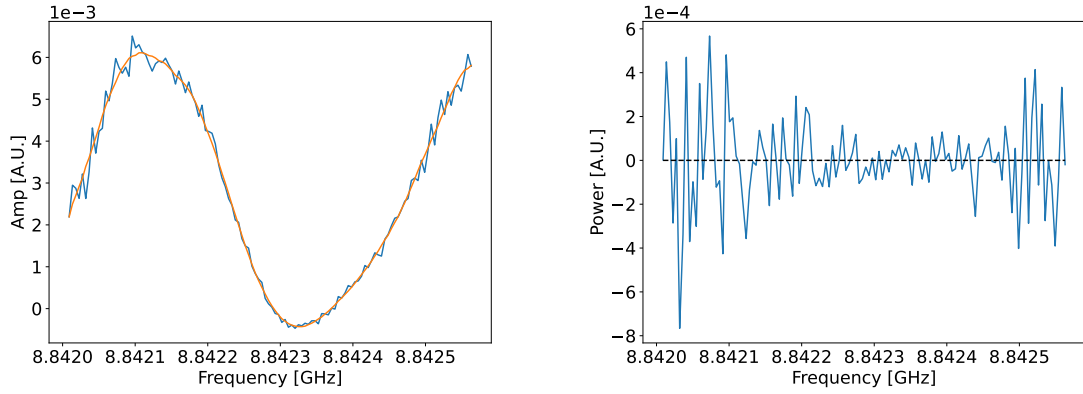


Figure 6. Left: in blue the weighted GUS δ_k^g . The distribution is inconsistent with a statistical noise distribution. The SG fit appears in orange. Right: final weighted GUS δ_k^f resulting from the subtraction of the left spectrum by its SG fit.

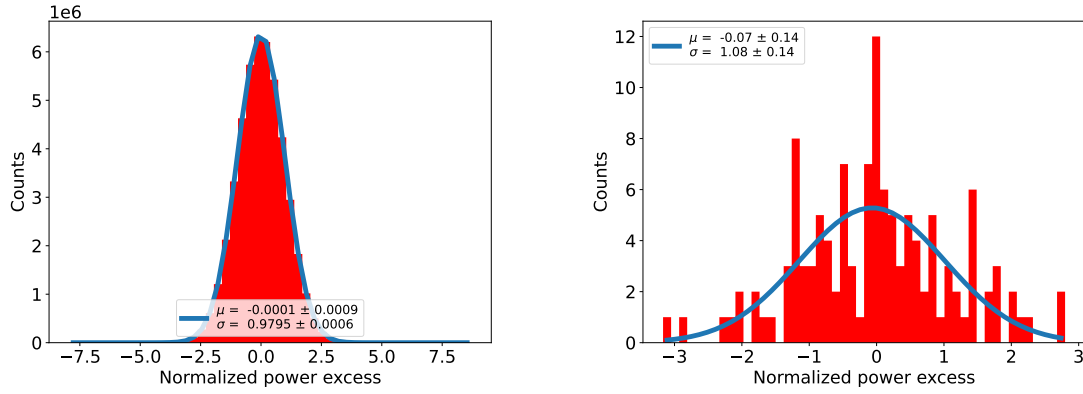


Figure 7. Left: histogram for all δ_{ij}^n/σ . Right: normalised histogram of the weighted GUS.

4 Results

We now proceed to analyse the section of the GUS that has the highest signal-to-noise ratio and is therefore most interesting to limit any possible presence of an axion signal. We choose a frequency interval to cover the tuning range of the central frequency of the cavity in the data set that we have analysed, plus the frequency interval for which the sensitivity drops by 3 dB from the maximum of the Lorentzian peak, on either side. This corresponds to a total frequency interval of 554 kHz, from approximately 8.842 01 GHz to 8.842 56 GHz, shown in the r.h.s. of figure 6.

To test for the presence of any possible axion signal with the theoretically expected form of the axion line shape for our Galactic halo, we use a discretised version of the modelled axion line shape [47]:

$$D_q = \int_{\nu_a + (q-1)\Delta\nu}^{\nu_a + q\Delta\nu} f(\nu) d\nu, \quad (4.1)$$

where ν_a is the axion frequency, q labels the bin number, $\Delta\nu$ the resolution bandwidth and

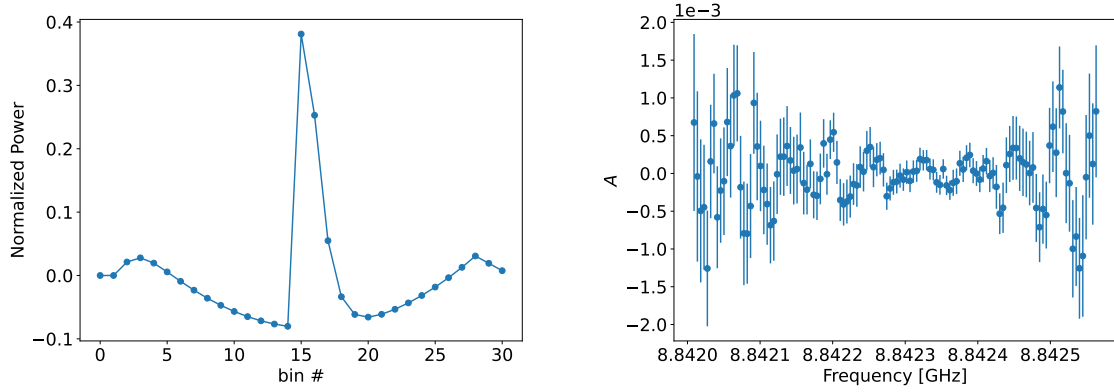


Figure 8. *Left:* normalised power of the distorted and attenuated axion line shape. *Right:* amplitude A (in units of normalised power excess) of the axion signal provided by the fit for each of the probed axion frequencies.

$f(\nu)$ is the normalised frequency line profile based on the standard isothermal spherical dark matter halo model [47, 50]. We then apply the same SG filter that is applied to the data to remove the systematic electronic residual in order to obtain the attenuated and distorted axion line shape (as described in [42]), D_q^d . The resulting model line profile is shown in the l.h.s. of figure 8.

This model fit function,

$$y = A \cdot D_q^d, \quad (4.2)$$

where A (the only free parameter in the fit) is the amplitude of the axion signal, is then used to search for an axion signal on the weighted GUS.

The r.h.s. of figure 8 shows the value of A obtained at each frequency step of width $\Delta\nu$. The largest excess in the amplitude plot has a 2.10σ local significance. A search including a misalignment ($\delta\nu_a$) within a bin width between the axion frequency ν_a and the DAQ k frequencies yielded the highest outlier at a local significance of 2.12σ only. Thus no significant signal above statistical fluctuations was observed.

The amplitude of the upper limit (A_{UL}) was computed using Bayesian statistics [25]:

$$\frac{1}{N} \int_0^{A_{\text{UL}}} e^{-(\sum_k S(\delta_k^f, A)/2)} dA = 1 - \alpha, \quad (4.3)$$

where N is the normalization factor, $S(\delta_k^f, A)$ is the χ^2 function (both given in [25]) and $1-\alpha$ is the credibility level (CL) of the upper limit. For this analysis a 95% CL was used.

By multiplying the A_{UL} values by the noise power ($P_N = k_b T_{\text{sys}} \Delta\nu$), we convert them into power values. An exclusion limit is established using:

$$A_{\text{UL}} \cdot P_N = P_a \quad (4.4)$$

and the conversion power P_a is given by:

$$P_a = g_{a\gamma}^2 \rho_a \frac{1}{m_a} B^2 V C \frac{\beta}{1+\beta} \min(Q_L, Q_a) \eta, \quad (4.5)$$

Parameter	Symbol	Value
Axion DM Density	ρ_a	0.45 GeV cm^{-3}
Total cavity volume	V	$(0.0288 \pm 0.0002) \text{ L}$
Magnetic field	B	$(11.7 \pm 0.1) \text{ T}$
Loaded quality factor	Q_L	$(36\,656 \pm 1832)$
Coupling factor	β	(0.81 ± 0.04)
Form factor	C	(0.634 ± 0.001)
Cable attenuation	η	(0.85 ± 0.04)
Noise Temperature	T_{sys}	$(6.7 \pm 0.8) \text{ K}$

Table 2. List of the environmental parameters used for the computation of the upper limit on the axion-photon coupling.

where $g_{a\gamma}$ is the axion-photon coupling, $\rho_a = 0.45 \text{ GeV cm}^{-3}$ [51] is the local dark matter density, m_a is the axion mass, B is the magnetic field strength, V is the volume of the cavity, Q_L and Q_a are the loaded cavity and axion quality factor respectively, C is the geometric factor, β is the coupling coefficient between the cavity and the receiver chain and η is the attenuation factor between the cavity output port and the LNA, which was estimated from the cable data sheet. Table 2 summarises the values used for this analysis. Note the largest error in these experimental parameters affecting our upper limits is that in T_{sys} , and that we do not include any error in the DM density ρ_a .

An exclusion limit between $g_{a\gamma} \gtrsim 6.3 \times 10^{-13} \text{ GeV}^{-1}$ and $g_{a\gamma} \gtrsim 1.59 \times 10^{-13} \text{ GeV}^{-1}$ was obtained for the range $36.5676 \mu\text{eV} < m_a < 36.5699 \mu\text{eV}$. The error propagation of the experimentally determined physical quantities included in equation (4.5) is used to determine the magnitude of the systematic uncertainties. These uncertainties are represented as the green band in the insert of figure 9. They were disregarded in the estimation of the exclusion limit since they account for less than 10% of the error.

Figure 9 shows the result of this analysis in the context of other haloscope searches: a competitive limit is set by RADES at an axion mass slightly lower than the QUAX results [19, 29, 52] and above the highest ADMX-Sidecar limit [53].

5 Conclusions

This work presents the analysis and results of the first data-taking campaign of the RADES group with a superconducting RF cavity. The use of a ReBCO taped cavity increased the quality factor compared to an usual copper coating by 50 %. Other studies have shown that this type of superconducting coating can yield an even higher increase of the quality factor, but this was limited here due to the 9 mm curvature radius of the cavity corners. There is a pathway we have started to overcome these limitations. Firstly, we are changing the tape provider to Fujikura, which has a critical bending radius smaller than the bending radius of the cavity. Together with an upgraded coating procedure for a new cavity we demonstrated a quality factor improvement by a factor of five with no magnetic field applied [63]. Secondly, if one wants to reach even higher quality factors, there are two main aspects that have

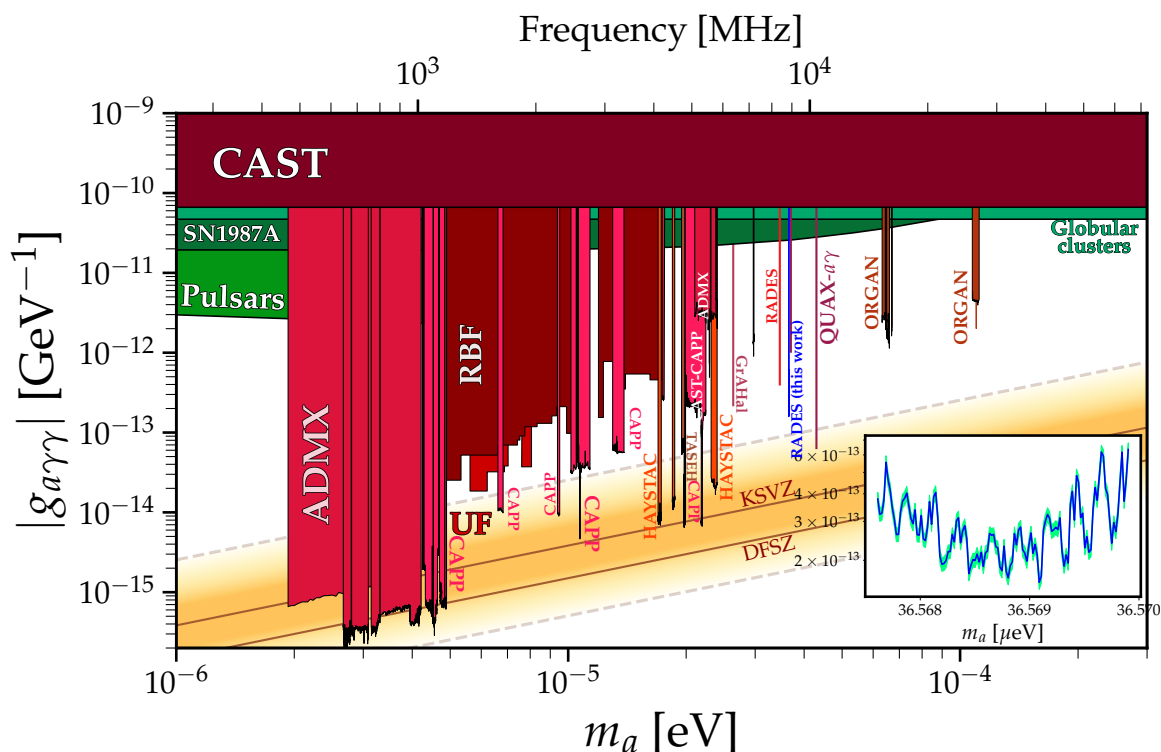


Figure 9. Axion mass versus axion-photon coupling phase-space. In blue the RADES axion-photon coupling exclusion limit with 95% credibility level presented in this article. Other haloscope results: RBF [54], UF [55], ADMX and ADMX-SideCar [16, 53, 56, 57], CAPP [17, 58, 59], HAYSTAC [18, 60], QUAX [19, 29, 52] and ORGAN [20, 61] and the CAST solar axion results [62] are plotted for comparison, see [11] for a full list of references and the raw source for the plot. Inset: zoom-in of the parameter range probed in this work ($36.5676 \mu\text{eV} < m_a < 36.5699 \mu\text{eV}$), where the green region represent the uncertainty of the measurement. The l.h.s. of the spectrum shows less sensitivity because fewer data were recorded at those frequencies.

to be replicated. (a) To operate in a Lorentz force-free configuration, that is where the B-field is parallel to most of the tape plane. (b) Avoid curved cavities as much as possible. In this regard, a polyhedral cavity that fulfils these two conditions has been designed for measurements in solenoid magnets. Thirdly, other steps will need to be done to reach the highest possible quality factors, such as polishing the sides of each facet of the polyhedral cavity to properly align them.

No signal excess has been found in the data analysed here when fitting the line-shape of a conventional axion dark matter halo model, in the range ($36.5676 \mu\text{eV} < m_a < 36.5699 \mu\text{eV}$) using 27 h of data. The obtained upper limit for the axion-photon coupling in our narrow frequency range is below the prior CAST limit [62] by more than two orders of magnitude. In addition, it improves the previous RADES search, which was made at a slightly lower cavity frequency, by a factor of 2.5 in the sensitivity to $g_{a\gamma\gamma}$. A difficulty encountered in our data analysis has been the presence of an excess of residual electronic systematics in the spectral analyser we used, which we have attempted to reduce using a Principal Component Analysis

Method. This has helped reduce the level of systematics but it has still caused problems in degrading our sensitivity; nevertheless, the problem should be resolved with improved equipment and experimental protocols in upcoming experiments in RADES.

Additional RADES R&D initiatives are under progress, including testing taller HTS-coated cavities as well as mechanical [64], ferroelectric and ferromagnetic tuning [65, 66] that should allow a search over a broader frequency range.

On the very long term, RADES envisages a data-taking in the magnet of the babyIAXO haloscope, with striking sensitivity in the 1-2 μeV mass range [67].

Acknowledgments

This project has received funding from the European Union’s Horizon 2020 Research and Innovation programme under Grant Agreement No 730871 (ARIES-TNA). This work has also received funding through the European Research Council under grant ERC-2018-StG-802836 (AxScale). IGI acknowledges funding through the European Research Council under grant ERC-2017-AdG-788781 (IAXO+).

This work has been partially funded by MCIN/AEI/10.13039/501100011033/ and by “ERDF A way of making Europe”, under grant PID2019-108122GB-C33, by PID2019-108122GB-C32, and by Maria de Maeztu program CEX2019-000918-M. JMGB thanks the grant FPI BES-2017-079787, funded by MCIN/AEI/10.13039/501100011033 and by “ESF Investing in your future”.

Generalitat Valenciana has also funded this work under the project ASFAE/2022/013.

The authors acknowledge the support and samples provided by THEVA.

ICMAB co-authors acknowledges funds from PID2021-127297OB-C21 and CEX2019-000917-S, FCC-GOV-CC-0208 (KE4947/ATS) and PRTR-C17I1 from MICIIN-NGEU-Generalitat de Catalunya.

We thank Giuseppe Ruoso for the loan of equipment and the CERN teams at SM18 and in the CERN Central Cryogenic Laboratory for the support, particularly: Gerard Willering, Franco Julio Mangiarotti, Jerome Feuvrier, Marta Bajko, Patrick Viret, Guillaume Pichon, Arnaud Devred, Stephan Russenschuck, Andrzej Siemko, Joanna Liberadzka-Porret and Torsten Koettig.

This research was supported by Deutsche Forschungsgemeinschaft (DFG) through Grant No. 532766533.

Data Availability Statement. This article has no associated data or the data will not be deposited.

Code Availability Statement. This article has no associated code or the code will not be deposited.

Open Access. This article is distributed under the terms of the Creative Commons Attribution License ([CC-BY4.0](https://creativecommons.org/licenses/by/4.0/)), which permits any use, distribution and reproduction in any medium, provided the original author(s) and source are credited.

References

- [1] R.D. Peccei and H.R. Quinn, *CP Conservation in the Presence of Instantons*, *Phys. Rev. Lett.* **38** (1977) 1440 [INSPIRE].
- [2] F. Wilczek, *Problem of Strong P and T Invariance in the Presence of Instantons*, *Phys. Rev. Lett.* **40** (1978) 279 [INSPIRE].
- [3] S. Weinberg, *A New Light Boson?*, *Phys. Rev. Lett.* **40** (1978) 223 [INSPIRE].
- [4] J. Ipser and P. Sikivie, *Are Galactic Halos Made of Axions?*, *Phys. Rev. Lett.* **50** (1983) 925 [INSPIRE].
- [5] M.S. Turner, F. Wilczek and A. Zee, *Formation of Structure in an Axion Dominated Universe*, *Phys. Lett. B* **125** (1983) 35 [Erratum *ibid.* **125** (1983) 519] [INSPIRE].
- [6] J. Preskill, M.B. Wise and F. Wilczek, *Cosmology of the Invisible Axion*, *Phys. Lett. B* **120** (1983) 127 [INSPIRE].
- [7] L.F. Abbott and P. Sikivie, *A Cosmological Bound on the Invisible Axion*, *Phys. Lett. B* **120** (1983) 133 [INSPIRE].
- [8] M. Dine and W. Fischler, *The Not So Harmless Axion*, *Phys. Lett. B* **120** (1983) 137 [INSPIRE].
- [9] V.B. Klaer and G.D. Moore, *The dark-matter axion mass*, *JCAP* **11** (2017) 049 [[arXiv:1708.07521](https://arxiv.org/abs/1708.07521)] [INSPIRE].
- [10] K. Saikawa, J. Redondo, A. Vaquero and M. Kaltschmidt, *Spectrum of global string networks and the axion dark matter mass*, *JCAP* **10** (2024) 043 [[arXiv:2401.17253](https://arxiv.org/abs/2401.17253)] [INSPIRE].
- [11] C. O'HARE, *Axion limits*, <https://github.com/cajohare/AxionLimits/>.
- [12] H. Primakoff, *Photoproduction of neutral mesons in nuclear electric fields and the mean life of the neutral meson*, *Phys. Rev.* **81** (1951) 899 [INSPIRE].
- [13] P. Sikivie, *Experimental Tests of the Invisible Axion*, *Phys. Rev. Lett.* **51** (1983) 1415 [Erratum *ibid.* **52** (1984) 695] [INSPIRE].
- [14] ADMX collaboration, *Axion Dark Matter Experiment: Detailed design and operations*, *Rev. Sci. Instrum.* **92** (2021) 124502 [[arXiv:2010.00169](https://arxiv.org/abs/2010.00169)] [INSPIRE].
- [15] I.G. Irastorza and J. Redondo, *New experimental approaches in the search for axion-like particles*, *Prog. Part. Nucl. Phys.* **102** (2018) 89 [[arXiv:1801.08127](https://arxiv.org/abs/1801.08127)] [INSPIRE].
- [16] ADMX collaboration, *Search for Invisible Axion Dark Matter in the 3.3–4.2 μ eV Mass Range*, *Phys. Rev. Lett.* **127** (2021) 261803 [[arXiv:2110.06096](https://arxiv.org/abs/2110.06096)] [INSPIRE].
- [17] C.M. Adair et al., *Search for Dark Matter Axions with CAST-CAPP*, *Nature Commun.* **13** (2022) 6180 [[arXiv:2211.02902](https://arxiv.org/abs/2211.02902)] [INSPIRE].
- [18] HAYSTAC collaboration, *A quantum-enhanced search for dark matter axions*, *Nature* **590** (2021) 238 [[arXiv:2008.01853](https://arxiv.org/abs/2008.01853)] [INSPIRE].
- [19] D. Alesini et al., *Search for Galactic axions with a high-Q dielectric cavity*, *Phys. Rev. D* **106** (2022) 052007 [[arXiv:2208.12670](https://arxiv.org/abs/2208.12670)] [INSPIRE].
- [20] A.P. Quiskamp et al., *Direct search for dark matter axions excluding ALPogenesis in the 63- to 67- μ eV range with the ORGAN experiment*, *Sci. Adv.* **8** (2022) abq3765 [[arXiv:2203.12152](https://arxiv.org/abs/2203.12152)] [INSPIRE].

- [21] J.M. García-Barceló, A. Díaz-Morcillo and B. Gimeno, *Enhancing resonant circular-section haloscopes for dark matter axion detection: approaches and limitations in volume expansion*, *JHEP* **11** (2023) 159 [[arXiv:2309.13199](#)] [[INSPIRE](#)].
- [22] J.M. García-Barceló et al., *Methods and restrictions to increase the volume of resonant rectangular-section haloscopes for detecting dark matter axions*, *JHEP* **08** (2023) 098 [[arXiv:2302.10569](#)] [[INSPIRE](#)].
- [23] MADMAX collaboration, *MADMAX - A Novel dielectric haloscope detector for post-inflationary axion dark matter searches*, *PoS ICHEP2022* (2022) 109 [[INSPIRE](#)].
- [24] ALPHA collaboration, *Searching for dark matter with plasma haloscopes*, *Phys. Rev. D* **107** (2023) 055013 [[arXiv:2210.00017](#)] [[INSPIRE](#)].
- [25] CAST collaboration, *First results of the CAST-RADES haloscope search for axions at 34.67 μ eV*, *JHEP* **10** (2020) 075 [[arXiv:2104.13798](#)] [[INSPIRE](#)].
- [26] F. Savary et al., *Design, Assembly, and Test of the CERN 2-m Long 11 T Dipole in Single Coil Configuration*, *IEEE Trans. Appl. Supercond.* **25** (2015) 4004105 [[INSPIRE](#)].
- [27] W. Chung, *Recent Progress on CAPP's Main eXperiment (CAPP-MAX)*, in proceedings of 18th Patras Workshop on Axions, WIMPs and WISPs, University of Rijeka, Rijeka, Croatia, 03–07 July 2023, <https://agenda.infn.it/event/34455/contributions/202514/>.
- [28] J. Golm et al., *Thin Film (High Temperature) Superconducting Radiofrequency Cavities for the Search of Axion Dark Matter*, *IEEE Trans. Appl. Supercond.* **32** (2022) 1500605 [[arXiv:2110.01296](#)] [[INSPIRE](#)].
- [29] D. Alesini et al., *Galactic axions search with a superconducting resonant cavity*, *Phys. Rev. D* **99** (2019) 101101 [[arXiv:1903.06547](#)] [[INSPIRE](#)].
- [30] D. Ahn et al., *Biaxially Textured YBa₂Cu₃O_{7-x} Microwave Cavity in a High Magnetic Field for a Dark-Matter Axion Search*, *Phys. Rev. Applied* **17** (2022) L061005 [[arXiv:2103.14515](#)] [[INSPIRE](#)].
- [31] A. Álvarez Melcón et al., *Scalable haloscopes for axion dark matter detection in the 30 μ eV range with RADES*, *JHEP* **07** (2020) 084 [[arXiv:2002.07639](#)] [[INSPIRE](#)].
- [32] W. Prusseit et al., *ISD process development for coated conductors*, *Physica C Superconductivity* **426** (2005) 866.
- [33] *ICMAB webpage*, <https://icmab.es/>.
- [34] A. Romanov et al., *High frequency response of thick REBCO coated conductors in the framework of the FCC study*, *Sci. Rep.* **10** (2020) 12325 [[INSPIRE](#)].
- [35] G.T. Telles et al., *Field quality and surface resistance studies of a superconducting REBa₂Cu₃O–Cu hybrid coating for the FCC beam screen*, *Supercond. Sci. Technol.* **36** (2023) 045001 [[INSPIRE](#)].
- [36] A. Romanov, *Superconducting Coated Conductors for Proton Beam Screens in High-Energy Particle Accelerators*, Ph.D. thesis, Universitat Autònoma de Barcelona, Barcelona, Spain (2022) [[INSPIRE](#)].
- [37] S. Otten, A. Kario, A. Kling and W. Goldacker, *Bending properties of different REBCO coated conductor tapes and Roebel cables at $T = 77$ K*, *Superconductor Science and Technology* **29** (2016) 125003.
- [38] J.W. Ekin, *Experimental techniques for low-temperature measurements: cryostat design, material properties and superconductor critical-current testing*, Oxford University Press (2006).

- [39] SolidWorks, *CST studio suite: Electromagnetic field simulation software*, <https://www.solidworks.com/de/media/cst-studio-suite-electromagnetic-field-simulation-software>.
- [40] Low Noise Factory, *Datasheet 6-20 GHz Cryogenic Low Noise Amplifier*, https://lownoisefactory.com/wp-content/uploads/2022/03/lmf-lnc6_20c.pdf.
- [41] Celestia TTI, *Radiofrequency and Antenna solutions*, <https://www.ttinorte.es/>.
- [42] S. Arguedas Cuendis, *Dark matter axion search using novel RF resonant cavity geometries in the CAST experiment*, Ph.D. thesis, University of Vienna, Vienna, Austria (2021) [INSPIRE].
- [43] Horizon Technologies, *Fluid property packages*, <https://htess.com/software-products/>.
- [44] D.M. Pozar, *Microwave engineering*, John Wiley & Sons (2011).
- [45] Rf microwave electronic components shop, *Datasheet of Semirigid PTFE Microwave Coaxial Cable - RG402-Cu*, <https://www.rf-microwave.com/en/qaxial/rg402-cu/semi-rigid-coaxial-cable-rg402-cu-50ohm-ptfe-3-58mm-5m/rg402-cu/>.
- [46] Keysight Technologies, *Application Note 5952-3706E (2019)*,
- [47] B.M. Brubaker et al., *HAYSTAC axion search analysis procedure*, *Phys. Rev. D* **96** (2017) 123008 [arXiv:1706.08388] [INSPIRE].
- [48] W.J. Krzanowski and J.E. Jackson, *A User's Guide to Principal Components*, *J. Roy. Statist. Soc. Series A* **155** (1992) 173.
- [49] A. Savitzky and M.J.E. Golay, *Smoothing and Differentiation of Data by Simplified Least Squares Procedures*, *Anal. Chem.* **36** (2002) 1627 [INSPIRE].
- [50] M.S. Turner, *Periodic signatures for the detection of cosmic axions*, *Phys. Rev. D* **42** (1990) 3572 [INSPIRE].
- [51] J.I. Read, *The Local Dark Matter Density*, *J. Phys. G* **41** (2014) 063101 [arXiv:1404.1938] [INSPIRE].
- [52] D. Alesini et al., *Search for invisible axion dark matter of mass $m_a = 43 \mu\text{eV}$ with the QUAX- $\alpha\gamma$ experiment*, *Phys. Rev. D* **103** (2021) 102004 [arXiv:2012.09498] [INSPIRE].
- [53] ADMX collaboration, *Piezoelectrically Tuned Multimode Cavity Search for Axion Dark Matter*, *Phys. Rev. Lett.* **121** (2018) 261302 [arXiv:1901.00920] [INSPIRE].
- [54] S. De Panfilis et al., *Limits on the Abundance and Coupling of Cosmic Axions at $4.5\text{-Microev} < m(a) < 5.0\text{-Microev}$* , *Phys. Rev. Lett.* **59** (1987) 839 [INSPIRE].
- [55] C. Hagmann, P. Sikivie, N.S. Sullivan and D.B. Tanner, *Results from a search for cosmic axions*, *Phys. Rev. D* **42** (1990) 1297 [INSPIRE].
- [56] ADMX collaboration, *Extended Search for the Invisible Axion with the Axion Dark Matter Experiment*, *Phys. Rev. Lett.* **124** (2020) 101303 [arXiv:1910.08638] [INSPIRE].
- [57] ADMX collaboration, *A Search for Invisible Axion Dark Matter with the Axion Dark Matter Experiment*, *Phys. Rev. Lett.* **120** (2018) 151301 [arXiv:1804.05750] [INSPIRE].
- [58] S. Lee et al., *Axion Dark Matter Search around $6.7 \mu\text{eV}$* , *Phys. Rev. Lett.* **124** (2020) 101802 [arXiv:2001.05102] [INSPIRE].
- [59] J. Jeong et al., *Search for Invisible Axion Dark Matter with a Multiple-Cell Haloscope*, *Phys. Rev. Lett.* **125** (2020) 221302 [arXiv:2008.10141] [INSPIRE].
- [60] HAYSTAC collaboration, *Results from phase 1 of the HAYSTAC microwave cavity axion experiment*, *Phys. Rev. D* **97** (2018) 092001 [arXiv:1803.03690] [INSPIRE].

- [61] B.T. McAllister et al., *The ORGAN Experiment: An axion haloscope above 15 GHz*, *Phys. Dark Univ.* **18** (2017) 67 [[arXiv:1706.00209](#)] [[INSPIRE](#)].
- [62] CAST collaboration, *New CAST Limit on the Axion-Photon Interaction*, *Nature Phys.* **13** (2017) 584 [[arXiv:1705.02290](#)] [[INSPIRE](#)].
- [63] J. Golm, *HTS RF cavities for axion searches and RADES update*, in proceedings of *Physics Beyond Colliders Annual Workshop*, CERN, Geneva, Switzerland, 07–09 November 2022 <https://indico.cern.ch/event/1137276/contributions/4950784>.
- [64] J. Golm et al., *Split-cavity tuning of a rectangular axion haloscope operating around 8.4 GHz*, *Front. in Phys.* **12** (2024) 1372846 [[arXiv:2312.13109](#)] [[INSPIRE](#)].
- [65] J.M.G. Barceló et al., *On the use of ferroelectric material in the detection of dark matter axions*, *IEEE Access* **11** (2023) 30360 [[arXiv:2204.11919](#)] [[INSPIRE](#)].
- [66] J.M. García-Barceló, *Development of resonant cavity-based microwave filters for axion detection*, PhD thesis, Technical University of Cartagena, Spain (2023).
- [67] S. Ahyoune et al., *A proposal for a Low-Frequency Axion Search in the 1–2 μeV Range and Below with the BabyIAXO Magnet*, *Annalen Phys.* **535** (2023) 2300326 [[arXiv:2306.17243](#)] [[INSPIRE](#)].